

Highly efficient continuous bistable nonlinear energy sink composed of a cantilever beam with partial constrained layer damping

Xin Fang · Jihong Wen · Jianfei Yin · Dianlong Yu

Received: 4 November 2015 / Accepted: 15 November 2016 / Published online: 2 December 2016
© Springer Science+Business Media Dordrecht 2016

Abstract This paper focuses on the transient nonlinear dynamics and targeted energy transfer (TET) of a Bernoulli–Euler beam coupled to a continuous bistable nonlinear energy sink (NES). This NES comprises a cantilever beam with the partial constrained layer damping (PCLD) and an end mass controlled by a nonlinear magnetostatic interaction force. The theoretical model of the nonlinear system is built based on the Lagrange equations and assumed-modes expansion method. A new parameter *system damping ratio* is proposed to evaluate the TET efficiencies. Impact experiments are carried out to verify the theoretical model and mechanisms. The results show that the bistable NES can achieve high and strongly robust TET efficiencies under broad-range impacts. The shear modulus of the viscoelastic layer, the length of the PCLD and the end mass have significant influences on TET efficiencies. Analyses of the TET mechanisms in the bistable NES show the following: steady transition of the stable state is an important reason for maintaining high TET efficiencies; nonlinear beatings can occur

in high-frequency, fundamental and long-period subharmonic branches; and resonance captures featuring fundamental and subharmonic also help achieve rapid energy dissipation.

Keywords Nonlinear dynamics · Bistable nonlinear energy sink · Transient impact · Continuous structure · Constrained layer damping · Vibration

1 Introduction

Vibration has large influences on the function, noise control and reliability of a mechanical system. Passive vibration control techniques have been chosen as a primary method in many facilities because of the advantages of high efficiency and lack of power consumption. The efficiencies of the traditional linear vibration absorbers or tuned mass dampers (TMDs) are restricted by their narrowband and poor robustness [1, 2]. A nonlinear approach for vibration suppression was considered to enable maintain high performance with a broader bandwidth under transient excitations. The passive nonlinear targeted energy transfer (TET) technique utilizes nonlinear mode localization and internal resonance to irreversibly transfer transient vibration energy from the primary system to a nonlinear energy sink (NES) that eventually dissipates the energy in the NES [3]. The robustness of an NES arises from the absence of the preferential linear natural frequency [4]. Research has been extensively investigated the phe-

Electronic supplementary material The online version of this article (doi:10.1007/s11071-016-3220-4) contains supplementary material, which is available to authorized users.

X. Fang · J. Wen (✉) · J. Yin · D. Yu
Laboratory of Science and Technology on Integrated Logistics Support, National University of Defense Technology, Changsha 410073, Hunan, China
e-mail: wenjihong@vip.sina.com

J. Yin
e-mail: nmhsyjf@hotmail.com

nomena and mechanisms of NES [5–7]. Fundamental TET, subharmonic TET and TET initiated by nonlinear beating are the main mechanisms, and nonlinear beating along the high-frequency special branches represents the most efficient mechanism of energy dissipation [8]. Presently, several types of NESs have been proposed and studied, such as oscillating dissipative attachments with essentially strong nonlinear stiffness [9–12], rotational elements [13, 14], vibro-impact NES [15, 16] and magnet-based NES [17]. Experiments have been carried out to verify the performance of NESs [18]. However, a traditional NES has a critical energy threshold in the transient regime in order to initiate the nonlinear beating [2, 8, 18], resulting in only having high TET efficiency under moderate transient impacts. Recently, a bistable NES [19, 20] was proposed to breakthrough the limit of the input energy threshold to maintain high performance of shock mitigation under a broad range of input energy. To explore the transient dynamics in a linear system coupled to a lightweight bistable mass, Romeo et al. [21] carried out a numerical study and Manevitch et al. [22] presented an analytical study with the complexification-averaging method [23]. Both studies focused on the impulsively excited linear oscillator (LO) to the bistable NES. The results show that, along with the main regime of 1:1 resonance capture, the superharmonic 1:3 resonance capture regime can also be realized and thus results in a strong energy exchange between the LO and bistable NES. However, the TET mechanisms and the nonlinear dynamics of the bistable NES need more research and experimental validations.

At present, a NES consists of a discrete single-degree-of-freedom (SDOF) nonlinear oscillator and a viscous damper. The transient dynamic behaviors of the SDOF NES coupled to a LO have been widely investigated. The only performance index of absorbers considered is the *percentage of instantaneous total energy dissipated by the NES*. However, this index percentage cannot reflect the decay rate of vibration energy that is an important parameter in practice. Recently, Farid and Gendelman [24] used the relative amount of the energy left in the system after a given time as an alternative index. Moreover, research on the NES composed of continuous structures is minimal. The bistable continuous structures were employed as vibration energy harvesters (VEHs) to achieve good performance under low-frequency excitations [25]. These VEHs usually consist of a cantilever beam attached with piezoelec-

tric generators. Most of the relevant literature modeled the bistable VEH as a SDOF oscillator by considering the first-order modal of the beam and considered the primary structures as rigid bodies [25–29]. However, these modeling methods are not proper for broad-range and high-frequency vibrations and cannot reveal the deformation of primary structures.

From the review above, it is important and interesting to study the nonlinear dynamics of a continuous elastic structure coupled to a continuous bistable NES. This paper focuses on the transient nonlinear dynamics and the TET efficiency of a continuous bistable energy sink coupled to an elastic beam. The NES consists of a cantilever beam attached with partial constrained layer damping (PCLD) and a magnetostatic field that produces an interaction force as the nonlinear restoring force. Based on the Lagrange equations and the assumed-modes expansion method, the motion differential equations are established to study the dynamic behaviors with numerical solutions. Besides the commonly used parameter *percentage of total energy dissipated by NES*, another parameter *system damping ratio* is defined to evaluate the TET efficiency. Impact experiments on the structure with different restoring forces are carried out to validate the theoretical model and the bistable transition behaviors. Then, the influences of different PCLD and structure parameters on TET efficiencies are investigated. Finally, this paper analyzes and summarizes the TET mechanisms of the bistable NES. There are five sections in this paper. The second section presents the process to establish the theoretical model and the analysis method. Impact experiments and comparisons between the experimental and theoretical results are described in Sect. 3. The efficiencies and mechanisms of the bistable NES are analyzed in Sect. 4 based on the numerical methods. Finally, we make conclusions in Sect. 5.

2 Modeling and derivation

2.1 Model description

The related systems are illustrated in Fig. 1. An NES is coupled to a primary Bernoulli–Euler beam (P-beam). Boundary conditions of the P-beam can be defined by its modal functions. The absorber consists of a small cantilever beam (S-beam) attached with PCLD and an end mass m_t . The magnetostatic interaction force of

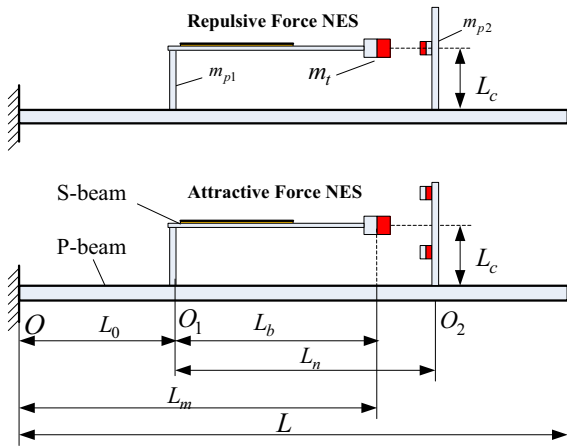


Fig. 1 The model of a monostable/bistable energy sink coupled to an elastic beam

the permanent magnets provides the nonlinear restoring force for the S-beam. There are two types of configurations: repulsive force and attractive force. Their modeling methods are identical; thus, only the attractive force NES is taken into account in the experiments and analyses. The S-beam is fixed to the P-beam at point O_1 with a rigid strut whose height is L_c . The other strut is fixed at point O_2 to support the magnets. For attractive force NES, the two smaller magnets on point O_2 are symmetrical to the undeformed S-beam. By modulating the magnetic forces, the absorber can behave as a monostable NES or a bistable NES. It is a linear absorber if the interaction force is zero. The masses of the struts are m_{p1} and m_{p2} , respectively. Other parameters are labeled in Fig. 1.

2.2 Magnetostatic interaction forces of permanent magnets

Traditionally, dipole–dipole magnetostatic interaction equations were used by most of the authors to incorporate the magnetic coupling induced into the dynamics of the energy harvesters [25–28]. However, the dipole–dipole formulation restricts the application within the sphere of its corresponding assumptions. Vokoun et al. [30,31] proposed the equations for magnetostatic forces between cylindrical permanent magnets. Avvari [32] used these equations to generate multi-stable states. With parameters labeled in Fig. 2b, the potential energy is [31,32]

$$E(D, y) = \varepsilon \mu_0 M_1 M_2 \pi R_2 R_1^2 \int_0^\infty J_0\left(\frac{yq}{R_1}\right) \frac{J_1(R_2q/R_1)}{q^2} J_1(q) U(D, q) dq \tag{1}$$

where $\varepsilon = -1$ ($\varepsilon = 1$) denotes the attractive (repulsive) force, μ_0 is the vacuum permeability $\mu_0 = 4\pi \times 10^{-7} \text{ N A}^{-2}$, R_i denotes the radii of the cylinders, $R_2 \leq R_1$ is assumed, M_1 and M_2 are the saturation magnetizations, and $J_0(\cdot)$ and $J_1(\cdot)$ are the zero-order and first-order Bessel functions, respectively. $U(D, q)$ is expressed as [32]

$$U(D, q) = e^{-q(d_1+d_2+D)/R_1} + e^{-qD/R_1} - e^{-q(D+d_1)/R_1} - e^{-q(D+d_2)/R_1}$$

$dJ_0(x)/dx = -J_1(x)$ and the interaction forces are obtained by $F_y(D, y) = -\partial E/\partial y$. Therefore, for the NES of the attractive force configuration, the total force in the transverse direction is

$$F_y(D, \Delta) = \mu_0 M_1 M_2 \pi R_1 R_2 \int_0^\infty \left[J_1\left(\frac{(d/2 - \Delta)q}{R_1}\right) - J_1\left(\frac{(d/2 + \Delta)q}{R_1}\right) \right] \frac{J_1(R_2q/R_1)}{q} J_1(q) U(D, q) dq \tag{2}$$

As analyzed in Fig. 3, Δ denotes the displacement of the end magnet on a cantilever beam relative to its undeformed point. Although $J_0(\cdot)$ and $J_1(\cdot)$ cannot be accurately expanded with few low-order terms of the Taylor series (order < 5), we can still accurately fit the force Δ curves described by (2) with a function $F_y(D, \Delta) = \varepsilon(\beta_1 \Delta + \beta_2 \Delta^3) + O(\Delta^5)$. Thus,

$$F_y(D, \Delta) \approx \beta_1 \Delta + \beta_2 \Delta^3 \tag{3}$$

One can use the polynomial fitting method to obtain parameters β_1 and β_2 . It can be deduced from equation (2) that the stiffness of β_1 and β_2 are correlative and that $\beta_1 > 0, \beta_2 < 0$.

2.3 Motion equations for NES coupled to an elastic beam

In engineering, the effectiveness of vibration control also depends on the damping configurations. Viscoelastic damping is widely adopted in continuous structures [33]. Constrained layer dampers (CLDs) were proposed by Edward and Kerwin [34]. The dissipation mechanisms of CLD mainly arise from the shear

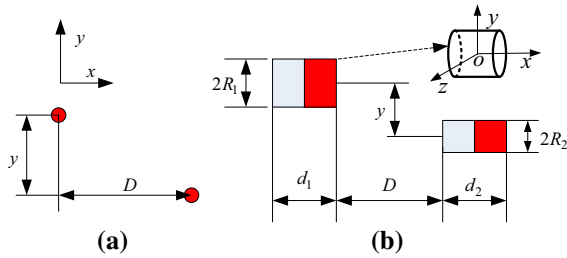


Fig. 2 Magnetostatic interaction in **a** dipole–dipole configuration and **b** cylinder–cylinder configuration

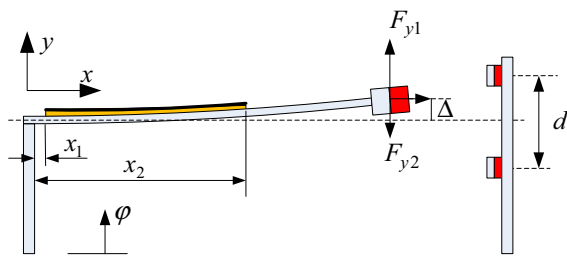


Fig. 3 Interaction forces generated by repulsive and attractive forces

deformation of the viscoelastic layer [33]. PCLD was proposed by Plunkett and Lee [35] to increase structural damping. Many researchers used the genetic algorithm method [36], moving asymptotes [37] and evolutionary structural optimization [38] to optimize the parameters of CLDs and PCLDs. This paper adopted unilateral PCLD to realize the damping of NES. The analytical calculations of CLD and PCLD are based on modal strain energy approaches proposed by Mead et al. [39,40].

The basic assumptions for the analytical model are (1) the presence of shear strain in the base and constrained layers; the rotary inertia of all layers is negligible; (2) the presence of only shear stress but no normal stress in the viscoelastic layer; (3) the strain is small compared to the structure for both linear and nonlinear NES; (4) the slipping does not occurs at the interfaces between layers and the deformations at the interfaces are continuous; (5) the plane transverse to the middle layer cross section remains planar during bending; and (6) the transverse displacements of all layers are identical. Based on these assumptions, the deformation patterns of the base beam, viscoelastic layer and constrained layer are illustrated in Fig. 4.

The geometry functions of displacements are

$$u_c = u_v + h_v (\gamma - \theta)/2 - h_c \theta/2$$

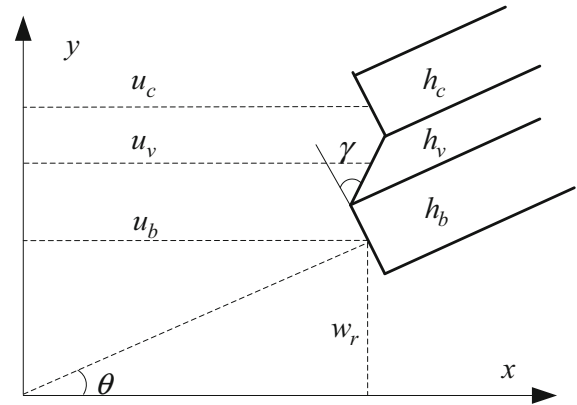


Fig. 4 Deformation pattern of three layers in PCLD treatment

$$u_b = u_v - h_v (\gamma - \theta)/2 + h_b \theta/2 \tag{4}$$

where subscripts ‘b’, ‘v’ and ‘c’ denote the base beam of the absorber, the viscoelastic layer and the constrained layer, respectively; u_b , u_v and u_c are longitudinal displacements (in x direction) of middle planes; w_r is the transverse displacement of the base beam relative to point O_1 in Fig. 1, and angle $\theta = \partial w_r / \partial x$; γ denotes the angle of the transverse plane of viscoelastic layer relative to its transverse direction; and h_b , h_v , and h_c represent the heights of the corresponding layers. Solving Eq. (4) obtains

$$u_v = \frac{u_b + u_c}{2} + \frac{h_c - h_b}{4} \frac{\partial w_r}{\partial x}$$

$$\gamma = \frac{1}{h_v} \left[u_c - u_b + h_t \frac{\partial w_r}{\partial x} \right], h_t = \frac{h_c + h_b + 2h_v}{2} \tag{5}$$

Assuming that the longitudinal displacement of the P-beam is negligible, the P-beam has a transverse displacement $y(x, t)$ only. Because the strut connecting the P-beam and the S-beam is rigid, the displacements and angles for the two beams should be identical at point O_1 . Assuming the displacement at point O_1 is $\varphi(t) = y(L_0, t)$, the absolute displacement of the S-beam is

$$w(x, t) = w_r + \varphi + x \sin \theta_0 \approx w_r + \varphi + x \frac{\partial y(L_0, t)}{\partial x} \tag{6}$$

where x is the distance between the point on the S-beam and its root O_1 . For the P-beam, a further assumption is made that additional mass m_{pi} are scattered at positions L_{xi} .

When the absorber is coupled to the P-beam, the kinetic energy of the entire system is

$$T = T_p + T_b + T_v + T_c + T_m \tag{7}$$

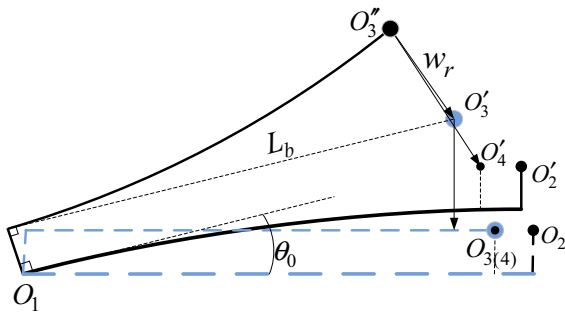


Fig. 5 Relationships between displacements

The subscripts ‘*p*’ and ‘*m*’ denote the P-beam and the end mass m_t , respectively. The expressions for T_p, T_b, T_v, T_c and T_m are shown in Appendix.

The potential energy of the system includes two parts: the strain energy of structures and the magnetostatic potential energy generated by force $F_y(D, \Delta)$ in Eq. (3). The strain potential energy of the P-beam, the base beam of absorber and the constrained layer are

$$\begin{aligned}
 V_p &= \frac{1}{2} \int_0^L E_p I_p \left(\frac{\partial^2 y(x, t)}{\partial x^2} \right)^2 dx \\
 V_b &= \frac{1}{2} \int_0^{L_b} \left[E_b A_b \left(\frac{\partial u_b}{\partial x} \right)^2 + E_b I_b \left(\frac{\partial^2 w_r}{\partial x^2} \right)^2 \right] dx \\
 V_c &= \frac{1}{2} \int_{x_1}^{x_2} \left[E_c A_c \left(\frac{\partial u_c}{\partial x} \right)^2 + E_c I_c \left(\frac{\partial^2 w_r}{\partial x^2} \right)^2 \right] dx
 \end{aligned} \tag{8}$$

where I_s, I_b and I_c represent the moment of inertia across the neutral surface of P-beam, the S-beam and the constrained layer, respectively, and they are $I_{b(c)} = bh_{b(c)}^3/12$, where b is the width. The shear strain energy of the viscoelastic layer is

$$V_v = \frac{1}{2} \int_{x_1}^{x_2} G_v A_v \gamma^2 dx \tag{9}$$

In Eqs. (8) and (9), $E_{p(b,c)}$ are elastic moduli and G_v is the shear modulus. These moduli are expressed as complex formats $E_{p(b,c)} = \bar{E}_{p(b,c)}(1+i\eta_{p(b,c)})$, $G_v = \bar{G}_v(1+i\eta_v)$, $i^2 = -1$, where $\eta_{p(b,c,v)}$ are loss factors.

The magnetostatic potential energy depends on the relative motion of magnets. As shown in Fig. 5, the end point of the undeformed S-beam falls at position O_3 . O_4 marks this point on the P-beam. After being deformed, O_3 moves to O'_3 , while O_4 moves to O'_4 , with a generated relative displacement $\Delta = |O'_3 O'_4|$. Seriously, $|O'_3 O'_4|$ is not a transverse displacement. In

practice, the distance D in Fig. 2b has a small alteration, and $|O'_3 O'_4|$ can be used to approximate this alteration. According to Eq. (6), Δ is expressed as

$$\begin{aligned}
 \Delta &= w(L_b, t) - y(L_m, t) = w_r(L_b, t) + y(L_0, t) \\
 &\quad + L_b \frac{\partial y(L_0, t)}{\partial x} - y(L_m, t)
 \end{aligned} \tag{10}$$

Defining $y_\Delta(t) = y(L_0, t) - y(L_m, t)$, then the magnetostatic potential energy generated by force $F_y(D, \Delta)$ is

$$\begin{aligned}
 V_m &= V_{m0} - \frac{1}{2} \beta_1 \left[w_r(L_b, t) + L_b \frac{\partial y(L_0, t)}{\partial x} + y_\Delta(t) \right]^2 \\
 &\quad - \frac{1}{4} \beta_2 \left[w_r(L_b, t) + L_b \frac{\partial y(L_0, t)}{\partial x} + y_\Delta(t) \right]^4
 \end{aligned} \tag{11}$$

in which $V_{m0} = E(D, 0)$ is the potential energy when the system is undeformed. Combining Eq. (5), the total energy is

$$V = V_p + V_b + V_v + V_c + V_m + V_{st0} \tag{12}$$

where V_{st0} is an artificial parameter added in the equation that makes the total potential energy zero when NES is positioned at its stable equilibrium at rest. One can obtain V_{st0} by making $V(t \rightarrow \infty) = 0$. For a certain absorber, V_{st0} is a unique constant. If there is only one stable equilibrium, $V_{st0} \equiv 0$.

This paper adopts the assumed-modes expansion method to investigate the nonlinear dynamics of monostable/ bistable NES. With the separation of variables, displacements are assumed to be

$$\begin{aligned}
 y(x, t) &= \sum_i^{n_s} Y_i(x) \phi_i(t) = \boldsymbol{\Phi}^T \mathbf{Y} \\
 w_r(x, t) &= \sum_{i=1}^{n_w} W_{ri}(x) \eta_i(t) = \boldsymbol{\eta}^T \mathbf{W}_r \\
 u_b(x, t) &= \sum_{i=1}^{n_b} U_{bi}(x) \xi_i(t) = \boldsymbol{\xi}^T \mathbf{U}_b \\
 u_c(x, t) &= \sum_{i=1}^{n_c} U_{ci}(x) \alpha_i(t) = \boldsymbol{\alpha}^T \mathbf{U}_c
 \end{aligned} \tag{13}$$

in which $Y_i(x), W_{ri}(x), U_{bi}(x)$ and $U_{ci}(x)$ are modal shape functions, and $\phi_i(t), \eta_i(t), \xi_i(t)$ and $\alpha_i(t)$ are the corresponding time functions of displacements. Then, letting $Y_{\Delta i} = Y_i(L_0) - Y_i(L_m)$, one obtains $y_\Delta(t) = \sum_i^{n_s} Y_{\Delta i} \phi_i(t)$.

Assuming that the distributed transverse loads $f_p(x, t)$ are applied on the P-beam and that $f_n(x, t)$

is applied on the S-beam, the generalized forces on the P-beam and S-beam can be calculated using

$$\begin{aligned} \mathbf{F}_p(t) &= \int_0^L f_p(x, t) \mathbf{Y}(x) dx \\ \mathbf{F}_n(t) &= \int_0^{L_b} f_n(x, t) \mathbf{W}_r(x) dx \end{aligned} \tag{14}$$

Subscript ‘*n*’ represents the NES or linear absorber. Usually, the external loads applied on the S-beam are zero.

The motion equations of the system can be set up with the Lagrange equations

$$\frac{d}{dt} \left(\frac{\partial T}{\partial \dot{q}_i} \right) - \frac{\partial T}{\partial q_i} + \frac{\partial V}{\partial q_i} = F_i, \quad i = 1, 2, \dots \tag{15}$$

in which q_i denotes the generalized modal coordinates in (13) and F_i represents the generalized force in (14). Substituting Eq. (13) into Eqs. (7) and (12) gives the total kinetic energy and potential energy. Then, we can calculate the motion differential function of the nonlinear system

$$\begin{aligned} \mathbf{M}_e \ddot{\mathbf{p}}(t) + \mathbf{K}_e \mathbf{p}(t) \\ - \beta_2 \left[w_r(L_b, t) + L_b \frac{\partial y(L_0, t)}{\partial x} + y_\Delta(t) \right]^3 \mathbf{P} = \mathbf{F}_e \end{aligned} \tag{16}$$

$$\begin{aligned} \mathbf{p}(t) &= \left[\boldsymbol{\phi}^T \quad \boldsymbol{\eta}^T \quad \boldsymbol{\xi}^T \quad \boldsymbol{\alpha}^T \right]^T \\ \mathbf{F}_e &= \left[\mathbf{F}_p(t)^T \quad \mathbf{F}_n(t)^T \quad 0 \quad 0 \right]^T \end{aligned} \tag{17}$$

In Eq. (16), \mathbf{M}_e and \mathbf{K}_e are the generalized mass and complex stiffness matrices, respectively. \mathbf{F}_e is the generalized excitation force vector. Subscript ‘*e*’ represents the ‘entire’ system. $\mathbf{p}(t)$ is the time function array of the displacement. \mathbf{P} is an array that represents the influence of nonlinear elements.

Both \mathbf{M}_e and \mathbf{K}_e are symmetrical block matrices, as listed in Appendix. $\mathbf{M}_{c\phi\phi}$ represents the coupling effect. The linear part of the magnetic force is exhibited in the matrices $\mathbf{K}_{\phi\eta}$ and $\mathbf{K}_{\eta\eta}$. If the bistable NES was not coupled to an elastic beam but was fixed on a rigid plane, all the terms relevant to $y(x, t)$ in the equations above are zero. In this situation, the motion differential equation for the standalone NES can be written as

$$\begin{aligned} \mathbf{M}_n \ddot{\mathbf{q}}(t) + \mathbf{K}_n \mathbf{q}(t) - \beta_2 w_r^3(L_b, t) \mathbf{P}_n = \mathbf{F}_n(t) \\ \mathbf{q}(t) = \left[\boldsymbol{\eta}^T \quad \boldsymbol{\xi}^T \quad \boldsymbol{\alpha}^T \right]^T \end{aligned} \tag{18}$$

\mathbf{M}_n and \mathbf{K}_n are also presented in Appendix.

2.4 Modal shape functions

Modal shape functions can be determined by boundary conditions. The P-beam is considered to be a cantilever beam whose modal shape functions are

$$\begin{aligned} Y_i(x) &= \cos g_i x - \cosh g_i x \\ &+ \frac{\sin g_i L - \sinh g_i L}{\cos g_i L + \cosh g_i L} (\sin g_i x - \sinh g_i x) \end{aligned} \tag{19}$$

with the eigenfunction $\cos gL \cosh gL = -1$. And $i = 1, 2 \dots n_p$. Other beams under different boundary conditions can be considered by choosing proper modal shape functions. For the S-beam in the absorber, the modal shape function of the transverse relative motion has the same form as (19) except the length is L_b . Its modal shape function of longitudinal motion is

$$U_b(x) = \sin \frac{(2i - 1)\pi x}{2L_b}, \quad i = 1, 2 \dots n_b \tag{20}$$

The constrained layer is considered as a free-free rod; therefore,

$$U_c(x) = \cos \frac{(i - 1)\pi x}{x_2 - x_1}, \quad i = 1, 2 \dots n_c \tag{21}$$

2.5 Damping transfer and definitions of TET efficiencies

Based on Eq. (16), for the linear system $\beta_1 = \beta_2 = 0$, the steady response formula under an excitation $\mathbf{F}_e = \bar{\mathbf{F}}_e e^{i\omega t}$ is $[\mathbf{K}_e - \omega^2 \mathbf{M}_e] \bar{\mathbf{p}} = \bar{\mathbf{F}}_e$. Then

$$\bar{\mathbf{p}} = \left[\mathbf{K}_e - \omega^2 \mathbf{M}_e \right]^{-1} \bar{\mathbf{F}}_e \tag{22}$$

substituting (22) into (13) provides the analytical solution for the steady response of the linear system. By comparing the analytical results with the linear finite element (FE) results, one can determine the proper DOF numbers for this research: being $n_p = 5, n_w = 6, n_b = n_c = 2$. This part of the content is presented in Supplementary material. The results also validate the accuracy of Eq. (22).

However, for the nonlinear NES that $\beta_1 \neq 0, \beta_2 \neq 0$, the solutions for both transient and steady responses become difficult because the DOF numbers are much larger than that of the 2DOF discrete oscillators. Numerical methods are adopted to solve the responses from the ordinary differential equations in (16) and (18). Because the imaginary part in the matrix \mathbf{K}_e

makes the numerical integration become non-convergent, we transform the structure damping model into a viscous damping model with an equivalent method. Decomposing the stiffness matrices into real and imaginary parts,

$$\mathbf{K}_e = \mathbf{K}_{er} + i \cdot \mathbf{K}_{ei}, \quad \mathbf{K}_n = \mathbf{K}_{nr} + i \cdot \mathbf{K}_{ni} \quad (23)$$

The imaginary part represents the damping effect. Under 1:1 resonance, one obtains

$$i \cdot \mathbf{K}_{ei}\mathbf{p}(t) = \frac{1}{\omega} \mathbf{K}_{ei}\dot{\mathbf{p}}(t) \quad (24)$$

Although the equivalent method (24) is under 1:1 resonance, it is also a valid approximation in other regimes. Under transient impact excitations, the system responses are mainly about the first-order natural frequency though higher-order modal responses still exist. Thus, one can replace the ω in Eq. (24) with the first natural frequency ω_{s1} of the P-beam. Defining the total damping matrix as $\mathbf{C}_e = \mathbf{K}_{ei}/\omega_{s1}$, then the motion equation can be expressed as

$$\mathbf{M}_e\ddot{\mathbf{p}}(t) + \mathbf{C}_e\dot{\mathbf{p}}(t) + \mathbf{K}_{er}\mathbf{p}(t) - \beta_2 \left[w_r(L_b, t) + L_b \frac{\partial y(L_0, t)}{\partial x} + y_\Delta(t) \right]^3 \mathbf{P} = \mathbf{F}_e \quad (25)$$

A similar treatment to Eq. (18) obtains

$$\mathbf{M}_n\ddot{\mathbf{q}}(t) + \mathbf{C}_n\dot{\mathbf{q}}(t) + \mathbf{K}_{nr}\mathbf{q}(t) - \beta_2 w_r^3(L_b, t)\mathbf{P}_n = \mathbf{F}_n(t) \quad (26)$$

Thereafter, the response of the nonlinear system can be accurately solved with the solver ode23t in MATLAB.

Simplifying expressions in (7) and (12), we obtain

$$T = \frac{1}{2} \dot{\mathbf{p}}(t)^T \mathbf{M}_e \dot{\mathbf{p}}(t) \\ V = \frac{1}{2} \mathbf{p}(t)^T \mathbf{K}_{er} \mathbf{p}(t) - \frac{1}{4} \beta_2 \Delta^4 + V_{st0} \quad (27)$$

The energy dissipated by the whole structure E_{ed} and by absorber E_{nd} in the time interval (t_0, t) is

$$E_{ed}(t) = \int_{t_0}^t \dot{\mathbf{p}}(\tau)^T \mathbf{C}_e \dot{\mathbf{p}}(\tau) d\tau \\ E_{nd}(t) = \int_{t_0}^t \dot{\mathbf{q}}(\tau)^T \mathbf{C}_n \dot{\mathbf{q}}(\tau) d\tau \quad (28)$$

Therefore, the *percentage of total impulse energy dissipated by the absorber* (or *energy dissipation percentage*) can be defined as

$$r_{dn} = E_{nd}/(E_{ed} + V_{st0}) \times 100\% \quad (29)$$

However, r_{dn} cannot reflect the decay rate of vibration energy that is also an important parameter in practice.

As is well understood, the response of a 1DOF linear oscillator under impact excitation has the form $y(t) = \bar{A}e^{-\lambda\omega_n t} \sin(\omega_d t + \theta)$ and $\omega_d = \omega_n\sqrt{1 - \lambda^2}$ [41], where ω_n is the natural frequency and λ is the critical damping ratio. For a continuous system, the amplitude follows the same rule. With an analogical method, the total energy of the NES system can be estimated as

$$E_e(t) = T + V \approx \bar{A}_E e^{-2\lambda\omega_{s1}t} \sin(2\omega_d t + \theta) \quad (30)$$

where ω_{s1} is the first natural frequency. The term $e^{-2\lambda\omega_{s1}t}$ plays the major role in amplitude decay in Eq. (30). Actually, the total energy can be always fitted with an exponential expression $E_e(t) \approx \bar{A}_E e^{-2\lambda\omega_{s1}t}$. Therefore, one can define λ as the *damping ratio of the entire system* that represents the decay rate of the impact energy. Then, the *system damping ratio* can be accurately evaluated when the responses of the system are calculated. In engineering, not only a large energy dissipation percentage but also high damping ratios are needed to protect the primary system.

2.6 Analysis of stable equilibriums

The stiffness of the absorber will increase after the S-beam is attached with the PCLD and becomes nonlinear when the magnetostatic force is applied at the end of the S-beam. The first-order nonlinear stiffness determines the number of stable equilibriums of the NES.

Firstly, the nonlinear NES coupled to a rigid body is considered. Assuming that a constant force $\bar{f}(x)$ is applied on point L_x , then $\mathbf{F}_n(t) = f_n \cdot \mathbf{s}(L_x)$, where $f_n(x, t) = \bar{f}(x)\delta(x - L_x)$, and the array $\mathbf{s}(L_x) = [W_{r1}(L_x) \dots W_{rn_w}(L_x) 0 \dots 0]^T$. By setting $\ddot{\mathbf{q}}(t) = 0$ in Eq. (26), one obtains $\bar{\mathbf{q}} = \bar{f} \cdot \mathbf{K}_{nr}^{-1} \mathbf{s}(L_x)$. Therefore, the deflection at point L_x is $\bar{w}_r = \bar{f} \cdot \mathbf{s}^T \mathbf{K}_{nr}^{-1} \mathbf{s}$. The first-order stiffness near the center point is

$$\tilde{k}_1 = \frac{\bar{f}}{\bar{w}_r} = \frac{1}{\mathbf{s}^T \mathbf{K}_{nr}^{-1} \mathbf{s}} \quad (31)$$

In practice, the NES is fixed to an elastic deformable structure. In this situation, the first-order stiffness k_1 of NES is smaller than \tilde{k}_1 . With array \mathbf{P} and the same approaches above, the equation is given by

$$k_1 = \frac{\bar{F}}{\bar{w}} = \frac{1}{\mathbf{P}^T \mathbf{K}_{er}^{-1} \mathbf{P}} \quad (32)$$

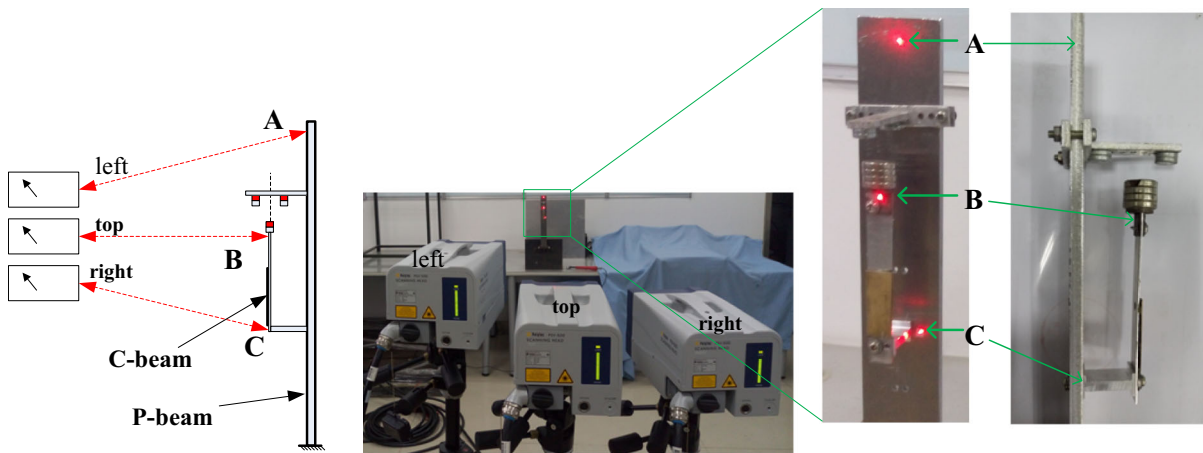


Fig. 6 Testing scheme and experiment setups

For a linear structure $\beta_1 = \beta_2 = 0$, one obtains the stiffness of the linear absorber k_0 with Eq. (32), $k_0 = k_1|_{\beta_1=0}$. For the pure cantilever beam without PCLD, its static stiffness is $k_{p0} = 3EI/L^3$. Because PCLD increases the stiffness, k_{p0} is smaller than k_0 , and a larger difference would occur for longer PCLD.

For nonlinear structures, the total restoring force for NES is $F_r(t) = k_1\Delta - \beta_2\Delta^3$ where $k_1 = k_0 - \beta_1$. Therefore, with specified parameters k_0 and β_1 , it is convenient to determine the stable state of NES based on k_1 . As stated before, $\beta_1 > 0$. If $\beta_1 \leq k_0$, $k_1 \geq 0$, although the magnetostatic force has a negative stiffness, the NES has single stable equilibrium that leads to a monostable NES. However, if $\beta_1 > k_0$, $k_1 < 0$, there will be three equilibriums on the occasion a bistable NES is obtained: the center unstable point and the other two stable equilibriums.

3 Experiments and comparisons

3.1 Experiment setups and parameters

The laser vibrometer Polytec-PSV-500 is used to measure the transient responses of the system. The testing scheme and experiment setup are illustrated in Fig. 6. Three vibrometers are employed to measure the vibration velocities at the three points, A, B and C, simultaneously. Point A is positioned at the end of the P-beam, point B is next to the endpoint of the S-beam, and point C is fixing point O_1 . The distance between B and C is 0.07 m. The modal hammer-2302 with a rubber head

is used to impact the P-beam at point A. The hammer's sensitivity is 2.5 mV/N.

The experiment parameters are listed in Table 1. Other parameters are as follows: the complex modulus of the viscoelastic layer $G_v = 3(1+0.1i)$ MPa; the position of the fixing point $L_0 = |OO_1| = 0.19$ m, as shown in Fig. 1; and the position of PCLD $x_1 = 0$, $x_2 = 0.03$ m, as shown in Fig. 3. The masses and positions of the two struts are $m_{p1} = 0.005$ kg and $L_{x1} = L_0$ and $m_{p2} = 0.016$ kg and $L_{x2} = L_0 + L_n$. With these parameters, we can calculate the stiffness of the linear absorber $\tilde{k}_0 = 454.47$ N/m and $k_0 = 453.26$ N/m. The end mass of the absorber is $m_t = 0.0156$ kg, $R_1 = 0.0075$ m, $R_2 = 0.005$ m, $d_1 = 0.012$ m, $d_2 = 0.004$ m and $d = 0.03$ m, as illustrated in Fig. 3. The saturation magnetizations are $M_1 = M_2 = 12.6 \times 10^5$ A/m.

3.2 Transient response of the cantilever beam coupled to a bistable NES

Before moving on to the nonlinear system containing bistable NES, three impact experiments were carried out on the pure P-beam, the P-beam coupled to a linear absorber and the P-beam coupled to a traditional monostable NES (Test-1 in Table 2), respectively. These experiments were conducted to verify the theoretical model for a linear and monostable NES under complex inputs and also to validate these parameters in part 3.1. Because the tested hammer impact forces contain a 'double hit,' the test forces were directly used

Table 1 Experiment parameters

Material properties	Primary beam (P-beam)	Base beam of absorber	Constrained layer	Viscoelastic layer
Elastic modulus (GPa)	70 (1 + 0.01 <i>i</i>)	70 (1 + 0.01 <i>i</i>)	49 (1 + 0.001 <i>i</i>)	–
Density ρ (kg/m ³)	2700	2700	7500	1000
Height <i>h</i> (m)	0.005	0.001	0.0004	0.00054
Length (m)	0.35	0.08	0.03	0.03
Width <i>b</i> (m)	0.04	0.012	0.012	0.012

Table 2 Additional experimental parameters for nonlinear restoring force

	<i>D</i> (mm)	β_1 (N/m)	$\beta_2 \times 10^6$ (N/m ³)	k_1 (N/m)
Test-1	11.2	255.83	−0.13654	197.43
Test-2	8.0	551.80	−2.8311	−98.740
Test-3	6.9	715.71	−3.6302	−262.46

as the input signals in the theoretical simulations to achieve a better comparison between the tests and theoretical results. These results are presented in Supplementary Materials.

With the same k_0 , the modulation of distance *D* generates different nonlinear dynamic properties. Additional parameters of the tests are provided in Table 2. The first test is monostable NES, and the second and the third tests are bistable NESs with different first-order stiffness k_1 . The fourth-order complex Gaussian wavelets are adopted in wavelet transforms (WTs).

Figures 7 and 8 illustrate the transient responses of the system in Test-2 under the impact amplitude of 40 N including the ‘double hit’ effects (as seen in the small iconography in Fig. 7b). As shown in Fig. 7a, b, the experimental and theoretical results are consistent in the initial stage; in the consequent motion, although they have differences in certain time ranges because of the frequency difference, the oscillating trends in the time domain and WTs are the same. A high-order response appears in the continuous NES, but it is not the major component. As seen in the theoretical phase diagram of point B, the distance between the two symmetrical stable equilibriums is 8.4 mm. However, the uncentering installation errors in the experiments cause the experimental phase diagram of point B to be asymmetrical. The bistable NES generates two jumps from one stable equilibrium to another one with a subharmonic frequency. This paper defines this phenomenon as the stable state transition. Combining the results of

WTs, the high-amplitude transition generates a 1:2 subharmonic nonlinear beating (during 0–0.3s) that results in highly efficient TET with a simultaneously rapid dissipation of energy. After the transition, motions of bistable NES are captured by one stable equilibrium. Additionally, vibrations in the primary system are largely weakened, and the 2:3 subharmonic resonance capture takes places to transfer energy to NES continuously. The subharmonic nonlinear beating observed in experiments is different from the high-frequency nonlinear beating occurring in traditional monostable NES.

In Test-3, both $|k_1|$ and $|\beta_2|$ are increased, but the wave of the impact force is similar to that of Test-2. As shown in Fig. 9a–c and Fig. 10a, b, the theoretical results exactly depict the vibration attenuation laws in this experiment. In (a) (b) (c) Figure 9c, the uncentering error still exists in the measurements. In this case, the distance between the two stable equilibriums increases to 13.8 mm, while the energy needed for the absorber to transition from one stable state to another one also increases. Therefore, the bistable NES in Test-3 only generates one transition under a similar impact. In the WTs plots, obvious components lower than 10 Hz during 0–0.2 s caused by the nonzero mean value rather than the vibration are observed. After a transient 1:1 resonance capture, energy localized in NES increases enough to drive the NES to transition and simultaneously bring a strong nonlinear beating following the 2:3 subharmonic orbit. During 0.3–1 s, continuous nonlinear beatings take place following the 1:1 resonance orbit. These nonlinear beatings generate highly efficient TET to suppress the vibration of the primary structure.

The analyses above indicate that the theoretical model established for continuous NES coupled to the elastic beam can accurately describe the dynamics of a linear system, monostable NES and bistable NES under complex impacts.

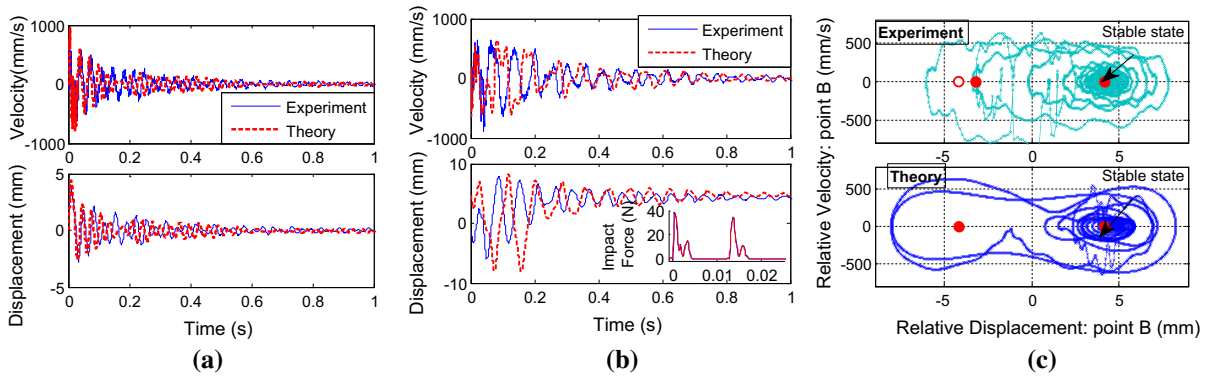


Fig. 7 Transient response of the system in Test-2. **a** Response at point A; **b** response at point B; **c** phase portraits of point B

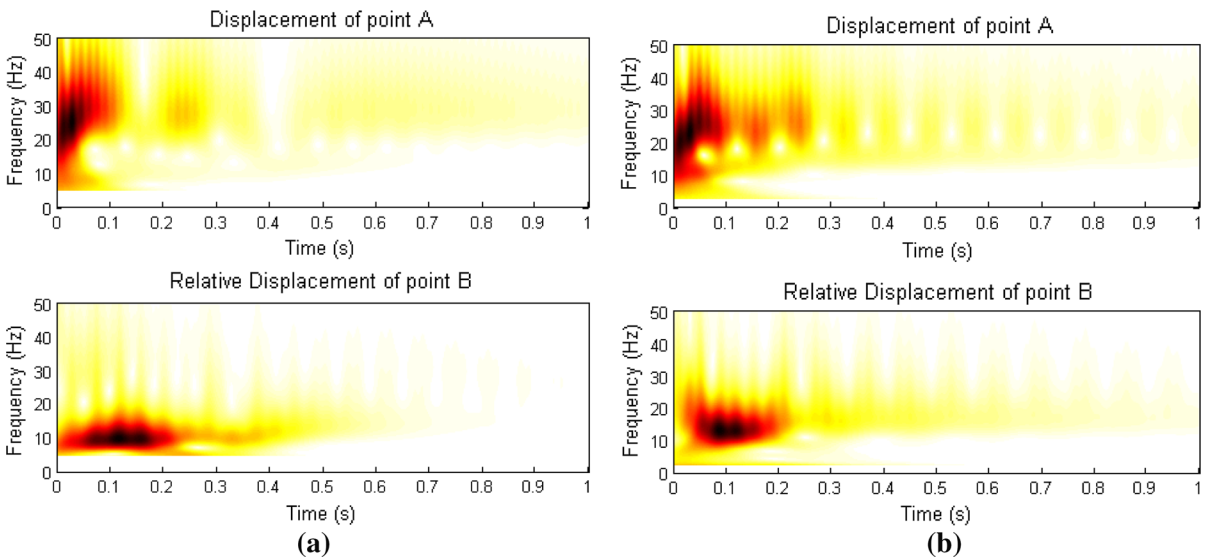


Fig. 8 Wavelet transforms of the response displacements in Test-2. **a** Theoretical results and **b** experimental results

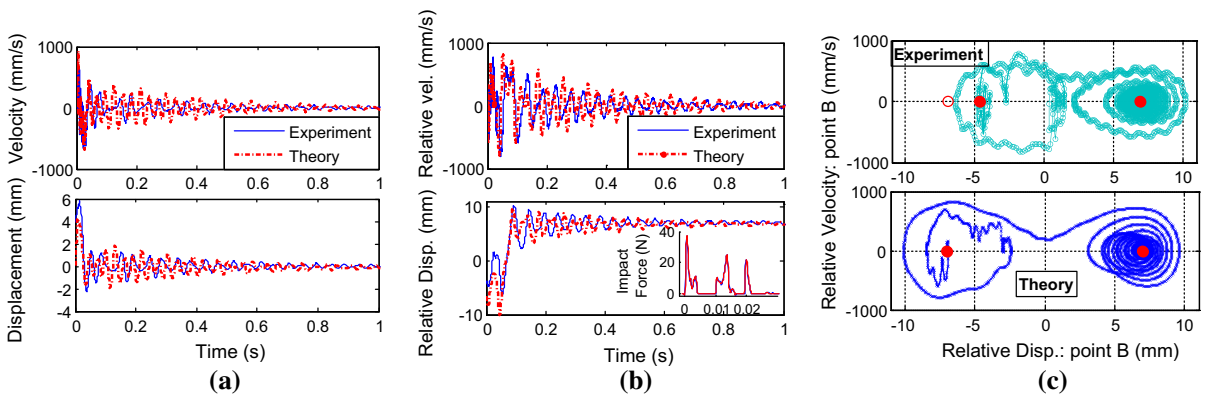


Fig. 9 Transient response of the system in Test-3. **a** Response at point A; **b** response at point B; **c** phase portraits of point B

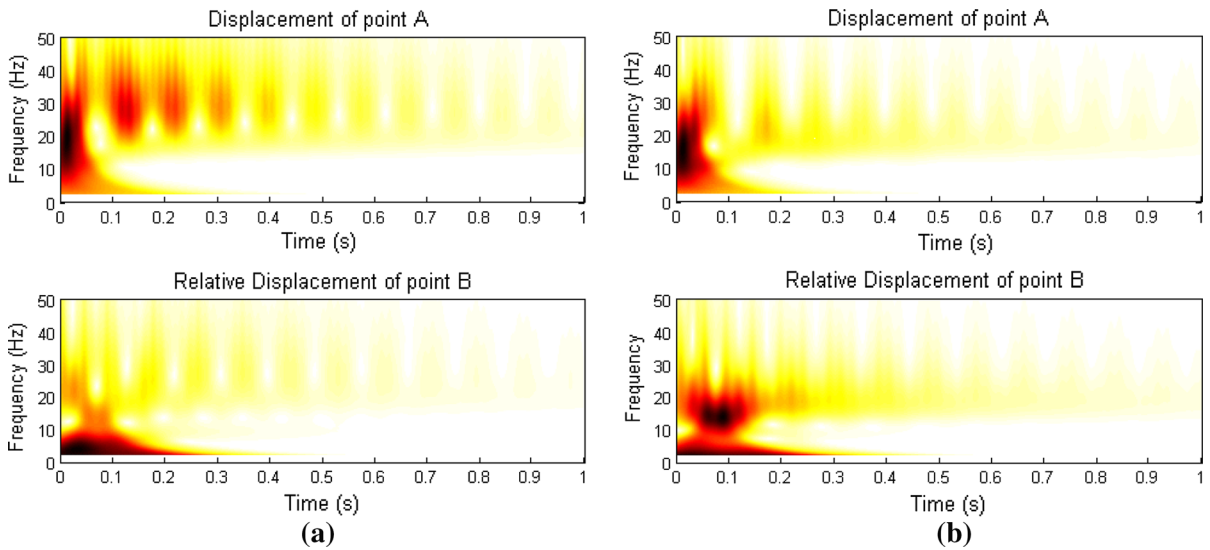


Fig. 10 Wavelet transforms of the response displacements in Test-3. **a** Theoretical results and **b** experimental results

4 TET efficiency and mechanisms

In this section, the TET efficiencies and TET mechanisms of bistable NES are discussed based on the theoretical model. Analysis of a large number of impact force signals generated by a hammer revealed that the width of a pulse is approximately 0.004 s. Therefore, the half sinusoidal pulses with a constant width of 0.004 s are used to simulate the impact forces on the P-beam.

4.1 TET efficiency of different absorbers

The TET efficiencies r_{dn} and λ of the linear absorber are independent on the input pulse. By modulating the elastic modulus E_b of the S-beam, TET efficiencies with different stiffness k_{s0} are illustrated in Fig. 11. The linear absorber is sensitive to the structure parameters, leading to poor robustness. Moreover, the parameter $E_b = 70$ GPa in the experiments in Sect. 3 is demonstrated to be the optimal choice for a linear structure ($r_{dn} = 66\%$, $\lambda = 0.016$) attached with a certain PCLD.

To explore the TET efficiency of an NES, a group of simulations are performed, as listed in Table 3. The structure parameters in Group 1 are identical with the parameters in the experiments. In the following contents, the numbers are labeled Gi-S-Nj and Gi-Bi-Nj. ‘Gi’ denotes the i th Group, ‘S-N’ denotes the traditional monostable NES, and ‘Bi-N’ represents the bistable NES.

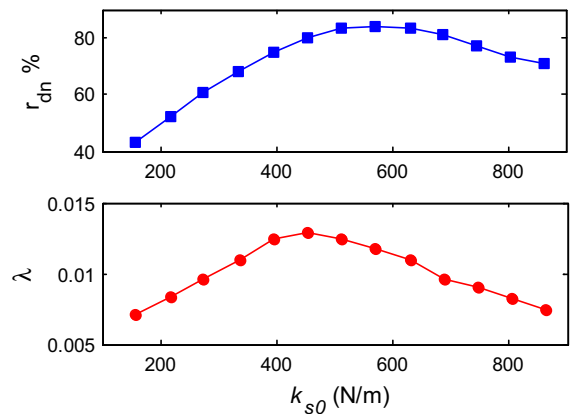


Fig. 11 TET efficiencies of linear absorbers with different stiffness k_{s0}

For bistable NES, there are two cases with opposite force directions, as shown in Fig. 12a. Taking G1-Bi-N2 as an example, Fig. 12b expatiates on the influence

Table 3 Parameters of restoring forces in Group 1

Numbers	D (mm)	β_1 (N/m)	$\beta_2 \times 10^6$ (N/m ³)	k_1 (N/m)
G1-Linear	–	0	0	453.26
G1-S-N1	9.85	354.56	–1.8621	98.74
G1-S-N2	9.5	403.19	–2.1044	50.07
G1-S-N3	8.82	453.26	–2.3515	0
G1-Bi-N1	8.37	504.26	–2.6037	–50.0
G1-Bi-N2	8.0	551.80	–2.8311	–98.74
G1-Bi-N3	7.2	666.31	–3.3924	–213.05

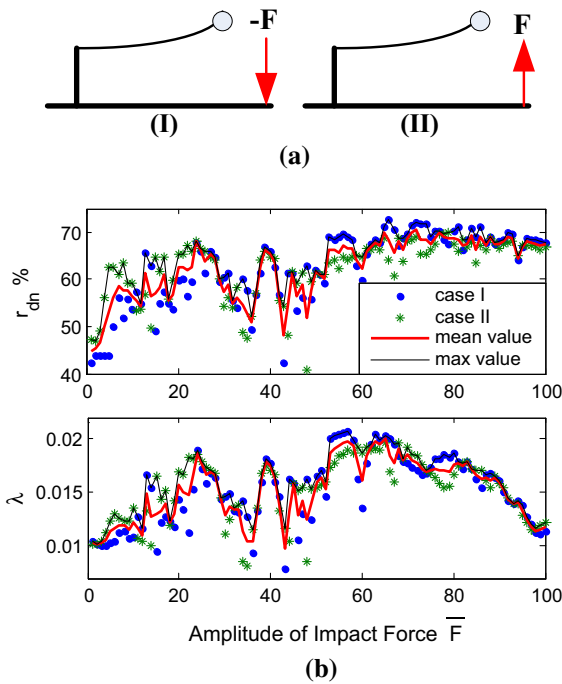


Fig. 12 TET efficiencies of bistable NES in two cases. **a** Two directions of excitation force and **b** TET efficiency

of force directions on the TET efficiencies. Both cases exhibit the sensitivity to the amplitudes of pulses, and TET efficiencies follow the same variation rule as a whole. When $1 < \bar{F} \leq 5\text{N}$, case II has higher r_{dn} and λ because the force in this direction excites a more efficient TET mechanism. When $\bar{F} > 65\text{N}$, the variation trends of r_{dn} and λ are different; λ decreases while r_{dn} maintains a high value as the pulse amplitude increases. The mean value of the two cases is calculated to evaluate the TET efficiencies of bistable NES in the following analyses.

TET efficiencies of different NESs in Group 1 are illustrated in Fig. 13. Under an extremely high-energy input ($\bar{F} > 100\text{N}$), deformations of the P-beam and S-beam would exceed the size and linearity limits, which is not considered in this paper. Because of the weak robustness of the linear absorber, 85% of the optimal values ($r_{dn} = 56\%$, $\lambda = 0.0136$) are also described. As shown in Fig. 13a, there is a critical threshold of impact amplitude, approximately 60 N, for highly efficient TET for monostable NESs. Under lower impacts, their efficiencies almost maintain constants and are much lower than the linear absorbers. In contrast, bistable NESs do not have the input threshold and can exceed the optimal efficiencies of the linear absorber in a wide

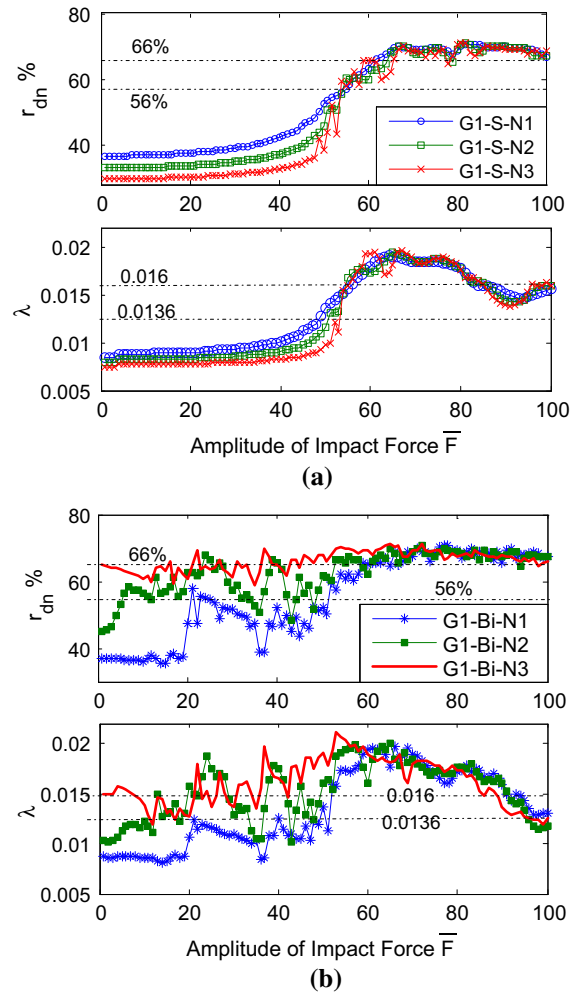


Fig. 13 TET efficiencies of different absorbers in Group 1. **a** Monostable NES and **b** bistable NES

impact range through modulating parameters. Moreover, the capacities for vibration attenuation of bistable NESs can be much better than monostable NESs under the middle-to-low amplitudes of impacts. The changing rules of TET efficiencies prove that the variation of r_{dn} is not consistent with that of λ under higher-energy input again.

4.2 Influences of structure parameters on TET efficiencies of bistable NES

We can interpret bistable NESs in terms of the influences of parameters on TET efficiencies of linear absorbers. The influences of G_v and h_v on the TET efficiencies of linear absorbers are shown in Supple-

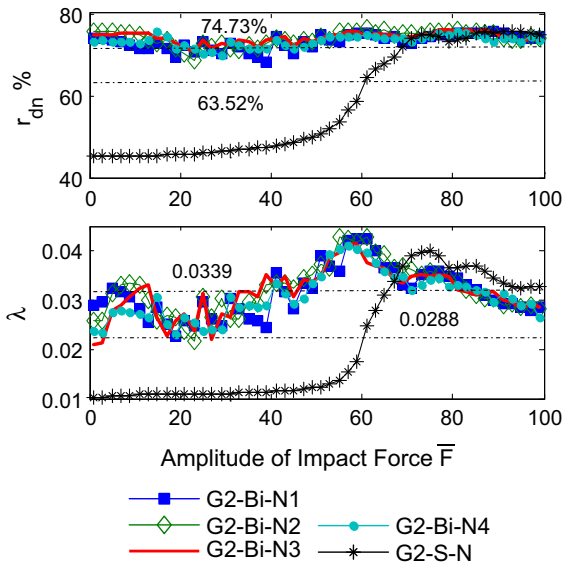


Fig. 14 TET efficiencies of absorbers in Group 2

mentary Material. From the results, a set of proper parameter $G_v = 6(1 + 0.1i)$ MPa and $h_v = 0.25$ mm (suboptimal values) are adopted for the simulations of the second group of bistable NESs. In this case, $k_0 = 489.16$ N/m, $r_{dn} = 74.73\%$, $\lambda = 0.0339$ for linear absorber and $d_2 = 6$ mm for nonlinear ones. The restoring force parameters in Group 2 are listed in Table 4 in Appendix.

The TET efficiencies of the five absorbers are illustrated in Fig. 14. Compared with Group 1, the TET efficiencies of bistable NESs get enhanced with the increase in the shear modulus of the viscoelastic layer and the damping ratios are enhanced much more. Efficiencies of the bistable NES are similar with the optimal linear absorber but are much better than the 85% of the optimal value. Although the stiffness changed remarkably, the efficiencies of the bistable NES remain steady with different impact amplitudes, indicating that an optimized NES has strong robustness.

With the parameters of G2-Bi-N2, influences of the length of PCLD with $x_1 = 0$ are investigated in Group 3. Its parameters are listed in Table 5 in Appendix. The results in Fig. 15 indicate that the PCLD length has important influence. Increasing the length will gain an additional energy dissipation percentage. However, when the length exceeds 30 mm, r_{dn} remains close to the upper limit of 80% although the PCLD length increases greatly. However, continuously increasing the length still significantly improves λ under small-

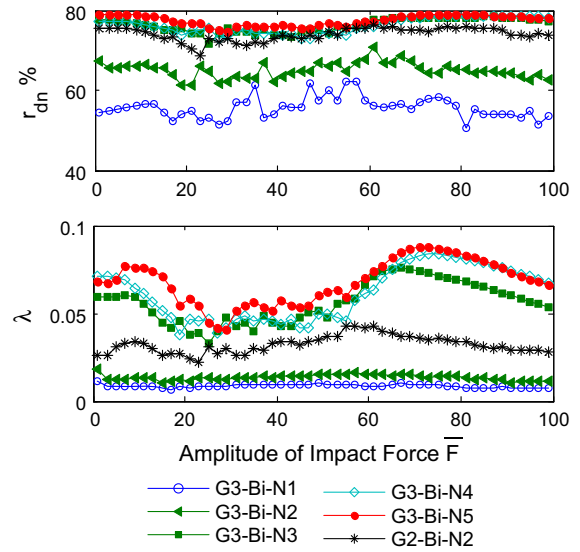


Fig. 15 TET efficiencies of bistable NESs in Group 3

and high-amplitude impacts. Moreover, modulating the nonlinear stiffness will improve the damping ratio further.

With the parameters of G2-Bi-N2, the influences of the end mass on TET efficiencies of bistable NES are shown in Fig. 16. The total mass of primary structures is $m_{pt} = m_p + m_{p1} + m_{p2} = 204.6$ g. The mass ratio is defined as $\varepsilon = m_t/m_{pt} \times 100\%$. Similar to the monostable NES, there is also a critical threshold for the small end mass continuous bistable NES (see the region $\bar{F} < 40$ N and $\varepsilon < 4\%$). Near $\varepsilon = 5\%$, r_{dn} reaches its optimal value, and there is a peak-value interval of $40 < \bar{F} < 70$ N for λ . This interval is to the right of the lowly efficient interval in Group 3, indicating that modulating the end mass can further optimize the bistable NES. However, the influences of the end mass are not monotonous; both r_{dn} and λ will decrease when ε increases continuously, and λ decreases faster.

In brief, the shear modulus of the viscoelastic layer, the PCLD length and the end mass of NES have important influences on the TET efficiencies of bistable NESs, and the system damping ratio is more easily affected.

4.3 TET mechanisms of bistable NES

Because of the strong nonlinearity, the TET mechanisms of bistable NES are much more complicated than that of the monostable NES. In recent publica-

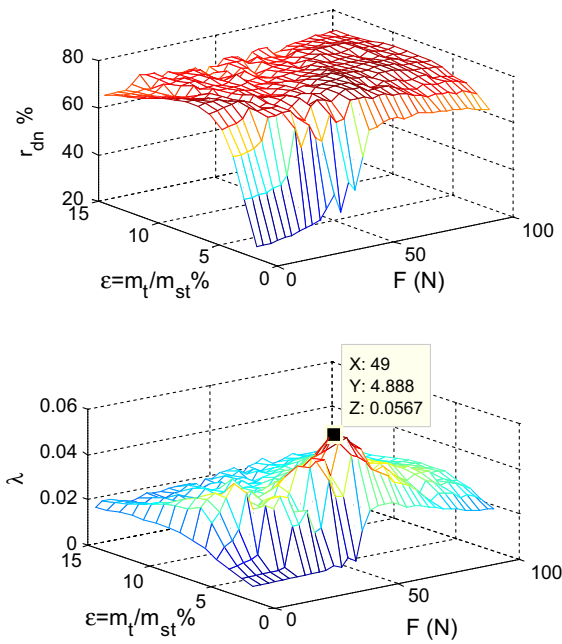


Fig. 16 Influences of end mass on TET efficiencies of bistable NES

tions [21,22], the main regimes considered in the discrete bistable oscillator are 1:1 and 1:3 resonance captures. Romeo et al. [20] found that the two main mechanisms in a discrete bistable NES are aperiodic (chaotic) cross-well oscillations and in-well nonlinear beats. In this section, nonlinear beating, fundamental and subharmonic resonance capture, and transitions of stable state are analyzed with examples in Group 1.

Under middle and higher-amplitude pulses, TET efficiencies of the bistable NES in Group 1 are steady. In the contents below, the relative displacement of NES denotes the point on the S-beam to be $x = L_b$. The WTs of displacements and the frequency energy plot (FEP) of the relative displacement under $\bar{F} = 80$ N are illustrated in Fig. 17. S_{mn} and U_{mn} (m and n are integers) are frequency orbits where the main frequency of the NES is $\omega = m\omega_{s0}/n$, $\omega_{s0} = 60\pi$. This paper decomposes S11 into S11+ and S11- but does not decompose other orbits as [3] did.

As shown in Fig. 17b, TET is initiated by high-frequency nonlinear beating following special orbits U65 to U32. Impact energy is transferred from low-frequency modes to high-frequency modes and is localized in NES. Therefore, the bistable NES gets a highly efficient TET. During 0.1–0.35 s, the mechanisms transform from the fundamental resonance capture along S11+ to subharmonic resonance capture

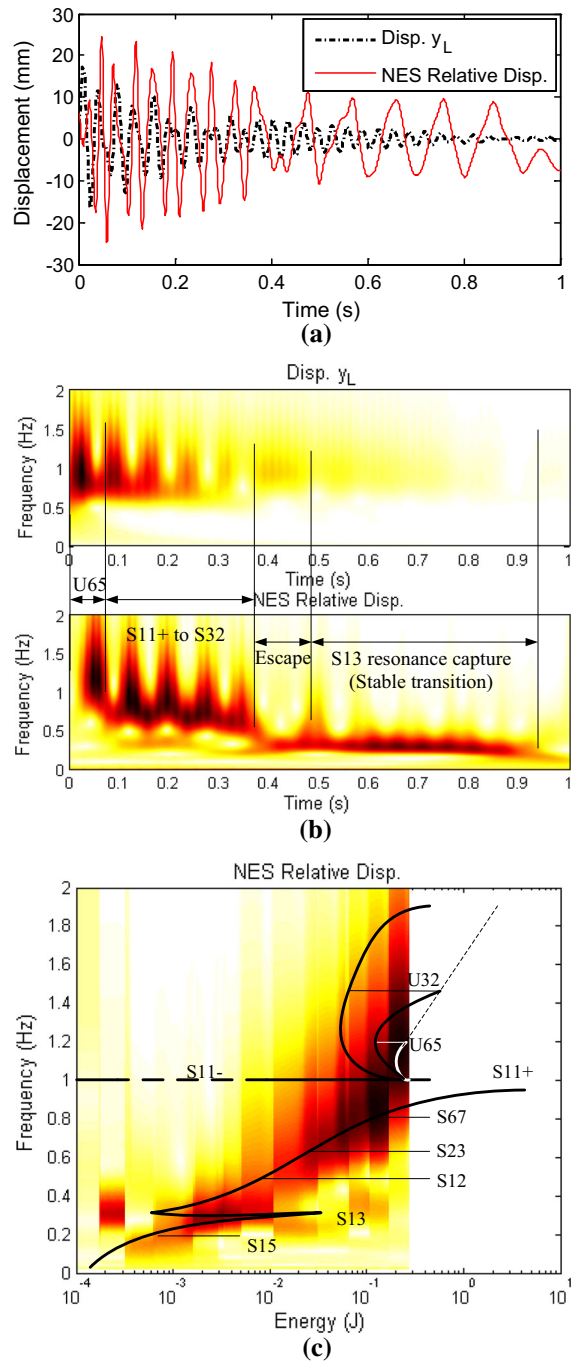


Fig. 17 WTs and FEP of G1-Bi-N2 under 80N. **a** Displacements; **b** WTs of the displacements; **c** FEP

along S23. Then, NES escapes from S23 and generates a steady 1:3 subharmonic resonance capture until there is not enough energy localized in NES to support its transition between two stable equilibria. During the subharmonic resonance capture, the low-amplitude

high-frequency vibration of the primary system drives the bistable NES to generate a high-amplitude low-frequency (HALP) response. Simultaneously, the high strain energy will dissipate the impact energy. The two stable equilibria attract the bistable NES generating steady transitions with higher amplitudes than the monostable ones.

When the impact energy decreases, the frequency of nonlinear beating is also reduced from high-frequency branches to 1:1 orbits. However, when the pulse amplitudes are lower than the critical threshold of monostable NES, the TET mechanism of monostable NES is 1:1 resonance capture along the orbit S11-, and nonlinear beatings disappear [3]. In contrast, bistable NES can still generate subharmonic responses because of the stable state transition. However, if the motions are captured by one stable state, the mechanisms will change.

Taking $\bar{F} = 41\text{N}$ as an example, results are shown in Fig. 18. In the initial stage before 0.1 s, energy transfer is initiated by a transient 1:1 fundamental resonance

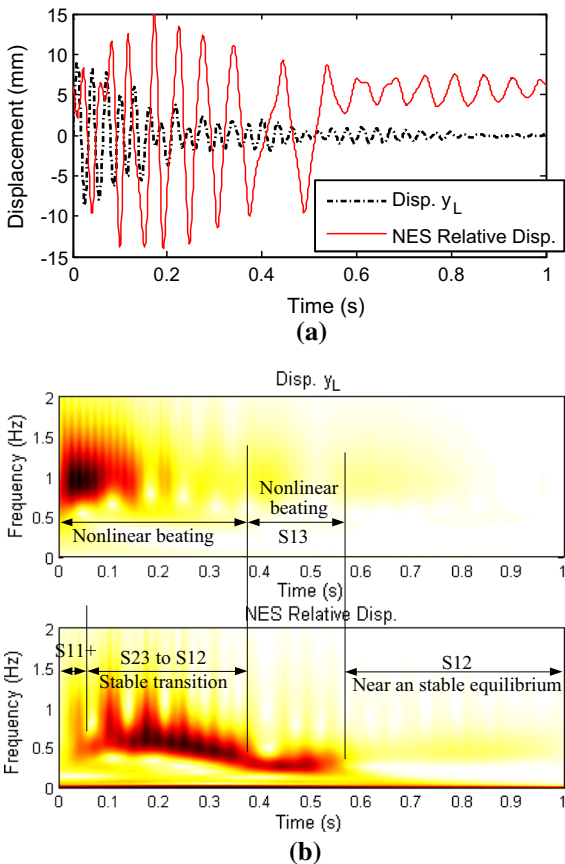


Fig. 18 Displacements and WT of G1-Bi-N2 under 41 N. **a** Displacements and **b** WT of displacements

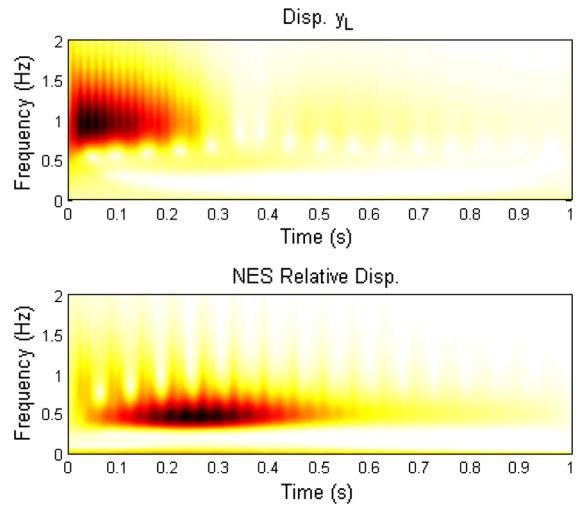


Fig. 19 WT of G1-Bi-N2 under case II $F = 5\text{ N}$ (case I $F = -5\text{ N}$ is presented in Supplementary material)

capture rather than the nonlinear beating. However, during 0.1–0.4 s, the bistable NES behaves as a HALP subharmonic response following S23 to S12; this is not the resonance capture but a long period of subharmonic nonlinear beating with the primary structure, making the energy irreversibly localized in bistable NES. Subsequently, another beating occurs along branch S13. The frequency of monostable NES monotonously decreases with energy. However, for a bistable NES, when the motions are captured by single stable equilibrium after 0.6 s, the responses of NES transfer from orbit S13 to S12, implying that the resonant frequency increases but the energy decreases. Figure 17c also illustrates this abnormal non-monotonic phenomenon.

Under small impacts, the NES motions are captured by single stable equilibrium. This situation is identical with that of the energy in NES attenuates from the transition to being captured by a stable equilibrium as shown above. Taking $F = 5\text{N}$ as an example, it generates a highly efficient long period of 1:2 subharmonic nonlinear beating, as illustrated in Fig. 19. Because the impact direction has influence on the TET efficiency in this case, $F = -5\text{N}$ results in lower efficiencies because the bistable NES under $F = -5\text{N}$ only generates a lowly efficient 1:1 resonance capture along orbit S11-, as shown in Fig. S7 See Supplementary Material. Under micro-impacts ($F \leq 1\text{ N}$), bistable NES behaves with similar dynamics with the linear absorber that generates a 1:1 beating along S11-, as shown in Fig. S8 See Supplementary Material. Therefore, different from traditional monostable NES, the orbit S11- is not

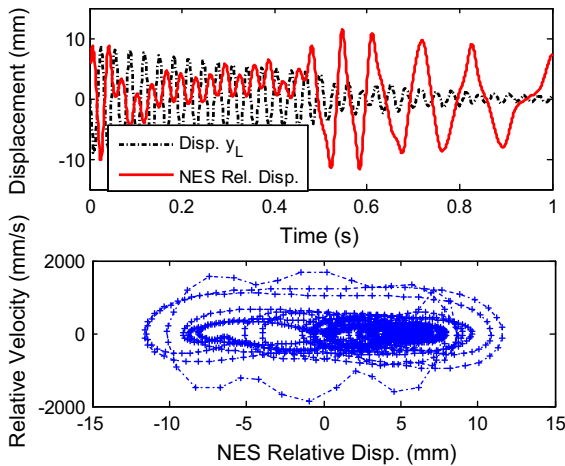


Fig. 20 Displacements and phase diagram of G1-Bi-N2 for $F = -43$ N

always a lowly efficient orbit for TET. Furthermore, a 1:1 resonance under low energy may not always exist. It depends on the parameters of NES and impact forces.

The work has analyzed the steady transition behaviors. However, for non-optimized bistable NES, because of the sensitivities to impact force, an unstable transition may appear. As shown in Fig. 20, before 0.5 s, there is 1:1 resonance, but the NES oscillates between a stable equilibrium and the unstable equilibrium. This is the unstable transition. Therefore, under a moderate-to-high impact, if unstable transition occurs in the initial stage of TET, the vibration attenuation efficient will be low. Subharmonic steady transition appears after 0.5 s, and then, the vibration of the primary beam is rapidly suppressed.

Based on the simulations above, the TET mechanisms of bistable NES are classified below.

1. Fundamental TET (S11+ and S11-)
2. Subharmonic resonance capture TET
3. TET initiated by nonlinear beating
 - 3.1 Fundamental nonlinear beating (beating along the orbit S11-). Occurs in the motions that captured by a stable equilibrium
 - 3.2 Subharmonic nonlinear beating along the branches S_{mn} , $m < n$
 - 3.3 Nonlinear beating along the high frequency branches U_{mn} , $m \geq n$. (occurs in the steady transition motions between the two stable equilibriums)
4. Unstable transition in initial stage

5 Conclusions

The investigated continuous system consists of a Bernoulli–Euler beam coupled to a continuous bistable NES. The NES comprises a cantilever beam with PCLD and an end mass controlled by a nonlinear magnetostatic interaction force. Both monostable and bistable NES can be achieved by modulating the nonlinear restoring force. This paper focuses on the transient nonlinear dynamics and TET efficiencies.

- (1) The motion differential equations of the system are established based on the Lagrange equations and assumed-modes expansion method. In addition to the *energy dissipation percentage*, a new index *system damping ratio* is proposed for evaluating TET efficiencies. The respective mean values of the two efficiency parameters in two opposite impact directions are calculated. Changing rules of the two parameters are not consistent, especially under large amplitude impacts.
- (2) Impact experiments on the linear absorber, monostable NES and bistable NES are gradually carried out to verify the theoretical model. The transition of the stable state, resonance capture and subharmonic nonlinear beating are observed in experiments. There are also high-order responses.
- (3) The monostable NES has to breakthrough a critical energy threshold to generate highly efficient TET. Bistable NES can achieve highly efficient and strongly robust TET under broad-range impacts. Efficiencies of bistable NESs are similar with the corresponding optimized linear absorber but are much better than the 85% of the optimal value. The impact directions influence the local but not the global properties of TET efficiencies. The shear modulus of the viscoelastic layer, the length of PCLD and the end mass have great influences on the TET efficiencies of bistable NESs, and the *system damping ratio* is more easily affected.
- (4) TET mechanisms in bistable NES are complex; nonlinear beating that achieves highly efficient irreversible TET can occur in high-frequency, fundamental and long-period subharmonic orbits. Resonance captures featuring fundamental and subharmonic also help achieve rapid energy dissipation. The steady transition of the stable state is an important reason for maintaining high efficiencies. However, an unstable transition may result in low

capacity for vibration attenuation. Furthermore, NES frequencies would not decrease monotonously with decreasing energy when motions are captured by a stable equilibrium.

We perform the conclusions about the mechanisms based on abundant numerical results (partially presented in this paper). An analytical proof would also be necessary to prove the results made in this study.

Acknowledgements This research was funded by the National Nature Science Foundation of China (Project Nos. 51405502 and 51275519). The authors would also like to acknowledge Associate Professor Yong Xiao and Doctor Xin Wang for their technical assistance.

Appendix

The kinetic energies of different parts can be expressed as

$$\begin{aligned}
 T_p &= \frac{1}{2} \int_0^L \left[\rho_p A_p + \sum_i m_{pi} \delta(x - L_{xi}) \right] \left(\frac{\partial y(x, t)}{\partial t} \right)^2 dx \\
 T_b &= \frac{1}{2} \int_0^{L_b} \rho_b A_b \left[\left(\frac{\partial w_r}{\partial t} + \dot{\varphi} + x \frac{\partial^2 y(L_0, t)}{\partial x \partial t} \right)^2 + \left(\frac{\partial u_b}{\partial t} \right)^2 \right] dx \\
 T_v + T_c &= \frac{1}{2} (\rho_v A_v + \rho_c A_c) \\
 &\quad \cdot \int_{x_1}^{x_2} \left(\frac{\partial w_r}{\partial t} + \dot{\varphi} + x \frac{\partial^2 y(L_0, t)}{\partial x \partial t} \right)^2 dx \\
 &\quad + \frac{1}{2} \int_{x_1}^{x_2} \left(\rho_v A_v \left(\frac{\partial u_v}{\partial t} \right)^2 + \rho_c A_c \left(\frac{\partial u_c}{\partial t} \right)^2 \right) dx \\
 T_m &= \frac{1}{2} m_t \left(\frac{\partial w_r(L_b, t)}{\partial t} + \dot{\varphi} + L_b \frac{\partial^2 y(L_0, t)}{\partial x \partial t} \right)^2 \\
 &\quad + \frac{1}{2} m_t \left(\frac{\partial u_b(L_b, t)}{\partial t} \right)^2 + \frac{1}{2} J_t \left(\frac{\partial^2 w_r(L_b, t)}{\partial x \partial t} \right)^2
 \end{aligned}$$

where J_t is the end mass's moment of inertia relative to the axis oz in Fig. 2b, $J_t = m_t R_1^2/4 + m_t d_1^2/12$.

The elements in the generalized mass matrix and generalized complex stiffness matrix are listed below.

$$\begin{aligned}
 \mathbf{M}_e &= \begin{bmatrix} \mathbf{M}_{\phi\phi} + \mathbf{M}_{c\phi\phi} & \mathbf{M}_{\phi\eta} & 0 & 0 \\ \mathbf{M}_{\phi\eta}^T & \mathbf{M}_{\eta\eta} & \mathbf{M}_{\eta\xi} & \mathbf{M}_{\eta\alpha} \\ 0 & \mathbf{M}_{\eta\xi}^T & \mathbf{M}_{\xi\xi} & \mathbf{M}_{\xi\alpha} \\ 0 & \mathbf{M}_{\eta\alpha}^T & \mathbf{M}_{\xi\alpha}^T & \mathbf{M}_{\alpha\alpha} \end{bmatrix} \\
 \mathbf{K}_e &= \begin{bmatrix} \mathbf{K}_{\phi\phi} & \mathbf{K}_{\phi\eta} & 0 & 0 \\ \mathbf{K}_{\phi\eta}^T & \mathbf{K}_{\eta\eta} & \mathbf{K}_{\eta\xi} & \mathbf{K}_{\eta\alpha} \\ 0 & \mathbf{K}_{\eta\xi}^T & \mathbf{K}_{\xi\xi} & \mathbf{K}_{\xi\alpha} \\ 0 & \mathbf{K}_{\eta\alpha}^T & \mathbf{K}_{\xi\alpha}^T & \mathbf{K}_{\alpha\alpha} \end{bmatrix}
 \end{aligned}$$

Table 4 Parameters of restoring forces in Group 2

Numbers	D (mm)	β_1 (N/m)	$\beta_2 \times 10^6$ (N/m ³)	k_1 (N/m)
G2-S-N	9.16	490	-2.0729	0
G2-Bi-N1	7.5	721	-3.3828	-231.84
G2-Bi-N2	7.2	775.54	-3.6324	-286.384
G2-Bi-N3	7	814.22	-3.8093	-325.064
G2-Bi-N4	6.8	854	-3.9952	-364.84

Table 5 Parameters for Group 3

	x_2 (mm)	k_0 (N/m)	k_1 (N/m)	$\beta_2 \times 10^6$ (N/m ³)
G3-Bi-N1	15	429.49	-346.054	-3.6324
G3-Bi-N2	20	444.76	-330.784	-3.6324
G2-Bi-N2	30	489.16	-286.384	-3.6324
G3-Bi-N3	40	547.4	-228.144	-3.6324
G3-Bi-N4	45	578.38	-197.164	-3.6324
G3-Bi-N5	45	854	-275.62	-3.9952

$$\begin{aligned}
 M_{\phi\phi,ij} &= \int_0^L \rho_p A_p Y_i Y_j dx + \sum_k m_{pk} Y_i(L_k) Y_j(L_k), \\
 &\quad i, j = 1, 2 \dots n_p
 \end{aligned}$$

$$\begin{aligned}
 M_{c\phi\phi,ij} &= \int_0^{L_b} \rho_b A_b [Y_i(L_0) + x Y_i'(L_0)] \\
 &\quad \cdot [Y_j(L_0) + x Y_j'(L_0)] dx + (\rho_c A_c + \rho_v A_v) \\
 &\quad \cdot \int_{x_1}^{x_2} [Y_i(L_0) + x Y_i'(L_0)][Y_j(L_0) + x Y_j'(L_0)] dx \\
 &\quad + m_t [Y_i(L_0) + L_b Y_i'(L_0)][Y_j(L_0) + L_b Y_j'(L_0)], \\
 &\quad i, j = 1, 2 \dots n_p
 \end{aligned}$$

$$\begin{aligned}
 M_{\phi\eta,ij} &= \int_0^{L_b} \rho_b A_b [Y_i(L_0) + x Y_i'(L_0)] W_{rj}(x) dx \\
 &\quad + \int_{x_1}^{x_2} (\rho_v A_v + \rho_c A_c) [Y_i(L_0) + x Y_i'(L_0)] W_{rj}(x) dx \\
 &\quad + m_t [Y_i(L_0) + L_b Y_i'(L_0)] W_{rj}(L_b), \\
 &\quad i = 1, 2 \dots n_p, j = 1, 2 \dots n_w
 \end{aligned}$$

$$\begin{aligned}
 M_{\eta\eta,ij} &= \int_0^{L_b} \rho_b A_b W_{ri} W_{rj} dx \\
 &\quad + \int_{x_1}^{x_2} (\rho_v A_v + \rho_c A_c) W_{ri} W_{rj} dx \\
 &\quad \cdot \int_{x_1}^{x_2} \rho_v A_v \frac{(h_c - h_b)^2}{16} W'_{ri} W'_{rj} dx \\
 &\quad + m_t W_{ri}(L_b) W_{rj}(L_b) + J_t W'_{ri}(L_b) W'_{rj}(L_b), \\
 &\quad i, j = 1, 2 \dots n_w
 \end{aligned}$$

$$M_{\eta\xi,ij} = \frac{1}{8} \int_{x_1}^{x_2} \rho_v A_v (h_c - h_b) W'_{ri} U_{bj} dx, \\ i = 1, 2 \dots n_w, j = 1, 2 \dots n_b$$

$$M_{\eta\alpha,ij} = \frac{1}{8} \int_{x_1}^{x_2} \rho_v A_v (h_c - h_b) W'_{ri} U_{cj} dx, \\ i = 1, 2 \dots n_w, j = 1, 2 \dots n_c$$

$$M_{\xi\xi,ij} = \int_0^{L_b} \rho_b A_b U_{bi} U_{bj} dx \\ + \frac{1}{4} \int_{x_1}^{x_2} \rho_v A_v U_{bi} U_{bj} dx + m_t U_{bi}(L_b) U_{bj}(L_b), \\ i, j = 1, 2 \dots n_b$$

$$M_{\xi\alpha,ij} = \frac{1}{4} \int_{x_1}^{x_2} \rho_v A_v U_{bi} U_{cj} dx, \\ i = 1, 2 \dots n_b, j = 1, 2 \dots n_c$$

$$M_{\alpha\alpha,ij} = \int_{x_1}^{x_2} \left(\rho_c A_c + \frac{1}{4} \rho_v A_v \right) U_{ci} U_{cj} dx, \\ i, j = 1, 2 \dots n_c K_{\phi\phi,ij} = \int_0^L E_p I_p Y'_i Y'_j dx \\ - \beta_1 (Y_{\Delta i} + L_b Y'_i) (Y_{\Delta j} + L_b Y'_j), \\ i, j = 1, 2 \dots n_p$$

$$K_{\phi\eta,ij} = -\beta_1 (Y_{\Delta i} + L_b Y'_i) W_{rj}(L_b), \\ i = 1, 2 \dots n_p, j = 1, 2 \dots n_w$$

$$K_{\eta\eta,ij} = \int_0^{L_b} E_b I_b W''_{ri} W''_{rj} dx + \int_{x_1}^{x_2} E_c I_c W''_{ri} W''_{rj} dx \\ + \int_{x_1}^{x_2} \frac{G_v A_v}{h_v^2} h_t^2 W'_{ri} W'_{rj} dx - \beta_1 W_{ri}(L_b) W_{rj}(L_b), \\ i, j = 1, 2 \dots n_w$$

$$K_{\eta\xi,ij} = - \int_{x_1}^{x_2} \frac{G_v A_v}{h_v^2} h_t W'_{ri} U_{bj} dx, \\ i = 1, 2 \dots n_w, j = 1, 2 \dots n_b$$

$$K_{\eta\alpha,ij} = \int_{x_1}^{x_2} \frac{G_v A_v}{h_v^2} h_t W'_{ri} U_{cj} dx, \\ i = 1, 2 \dots n_w, j = 1, 2 \dots n_c$$

$$K_{\xi\xi,ij} = \int_0^{L_b} E_b A_b U'_{bi} U'_{bj} dx + \int_{x_1}^{x_2} \frac{G_v A_v}{h_v^2} U_{bi} U_{bj} dx, \\ i, j = 1, 2 \dots n_b$$

$$K_{\xi\alpha,ij} = - \int_{x_1}^{x_2} \frac{G_v A_v}{h_v^2} U_{bi} U_{cj} dx, \\ i = 1, 2 \dots n_b, j = 1, 2 \dots n_c$$

$$K_{\alpha\alpha,ij} = \int_{x_1}^{x_2} E_c A_c U'_{ci} U'_{cj} dx + \int_{x_1}^{x_2} \frac{G_v A_v}{h_v^2} U_{ci} U_{cj} dx, \\ i, j = 1, 2 \dots n_c$$

$$P_i = \begin{cases} (Y_{\Delta i} + L_b Y'_i) & \text{for } i = 1, 2 \dots n_p \\ W_{ri}(L_b) & \text{for } i = n_p + 1, \dots n_p + n_w \\ 0 & \text{others} \end{cases}$$

$$M_n = \begin{bmatrix} M_{\eta\eta} & M_{\eta\xi} & M_{\eta\alpha} \\ M_{\eta\xi}^T & M_{\xi\xi} & M_{\xi\alpha} \\ M_{\eta\alpha}^T & M_{\xi\alpha}^T & M_{\alpha\alpha} \end{bmatrix},$$

$$K_n = \begin{bmatrix} K_{\eta\eta} & K_{\eta\xi} & K_{\eta\alpha} \\ K_{\eta\xi}^T & K_{\xi\xi} & K_{\xi\alpha} \\ K_{\eta\alpha}^T & K_{\xi\alpha}^T & K_{\alpha\alpha} \end{bmatrix}$$

References

1. Anubi, O.M., Crane III, C.D.: A new active variable stiffness suspension system using a nonlinear energy sink-based controller. *Vehicle Syst. Dyn.* **51**(10), 1588–1602 (2013)
2. Kremer, D., Liu, K.F.: A nonlinear energy sink with an energy harvester: transient responses. *J. Sound Vib.* **333**, 4859–4880 (2014)
3. Lee, Y.S., Vakakis, A.F., Bergman, L.A., McFarland, D.M., et al.: Passive non-linear targeted energy transfer and its applications to vibration absorption: a review. *Proc. IMechE. Part K J. Multi-Body Dyn.* **222**(2), 77–134 (2007)
4. Gourdon, E., Lamarque, C.H., Pernot, S.: Contribution to efficiency of irreversible passive energy pumping with a strong nonlinear attachment. *Nonlinear Dyn.* **50**, 793–808 (2007)
5. Gendelman, O.V.: Transition of energy to a nonlinear localized mode in a highly asymmetric system of two oscillators. *Nonlinear Dyn.* **25**, 237–253 (2001)
6. Vakakis, A.F.: Inducing passive nonlinear energy sinks in vibrating systems. *J. Vib. Acoust.* **123**, 324–332 (2001)
7. Vakakis, A.F., Gendelman, O.V.: Energy pumping in nonlinear mechanical oscillators: Part II-resonance capture. *J. Appl. Mech.* **68**, 42–48 (2001)
8. Vakakis, A.F., Gendelman, O.V., Bergman, L.A., McFarland, D.M., Kerschen, G., Lee, Y.S.: *Nonlinear Targeted Energy Transfer in Mechanical and Structural Systems*. Springer, Dordrecht (2008)
9. Lee, Y.S., et al.: Enhancing the robustness of aeroelastic instability suppression using multi-degree-of-freedom nonlinear energy sinks. *AIAA J.* **46**, 1371–1394 (2008)
10. Sapsis, T.P., et al.: Effective stiffening and damping enhancement of structures with strongly nonlinear local attachments. *J. Vib. Acoust.* **134**, 011016 (2012)
11. Quinn, D.D., et al.: Equivalent modal damping, stiffening and energy exchanges in multi degree-of-freedom systems with strongly nonlinear attachments. *Proc. Inst. Mech. Eng., Part K J. Multi-Body Dyn.* **226**(2), 122–146 (2012)
12. Gendelman, O.V., Sapsis, T., Vakakis, A.F., Bergman, L.A.: Enhanced passive targeted energy transfer in strongly nonlinear mechanical oscillators. *J. Sound Vib.* **330**, 1–8 (2011)
13. Gendelman, O.V., Sigalov, G., Manevitch, L.I.: Dynamics of an eccentric rotational nonlinear energy sink. *J. Appl. Mech.* **79**, 011012 (2012)
14. Sigalov, G., Gendelman, O.V., AL-Shudeifat, M.A., Manevitch, L.I., Vakakis, A.F., Bergman, L.A.: Resonance

- captures and targeted energy transfers in an inertially-coupled rotational nonlinear energy sink. *Nonlinear Dyn.* **69**, 1693–1704 (2012)
15. Gendelman, O.V.: Analytic treatment of a system with a vibro-impact nonlinear energy sink. *J. Sound Vib.* **331**, 4599–4608 (2012)
 16. Karayannis, I., Vakakis, A.F., Georgiades, F.: Vibro-impact attachments as shock absorbers. *Proc. IMechE. J. Mech. Eng. Sci.* **222**, 1899–1908 (2008)
 17. Mohammad, A., Shudeifat, A.L.: Asymmetric magnet-based nonlinear energy sink. *J. Comput. Nonlinear Dyn.* **10**(1), 014502 (2014)
 18. Wierschem, N.E.: Targeted Energy Transfer Using Nonlinear Energy Sinks for the Attenuation of Transient Loads on Building Structures. Ph.D. thesis (2014)
 19. Mohammad, A., Shudeifat, A.L.: Highly efficient nonlinear energy sink. *Nonlinear Dyn.* **76**, 1905–1920 (2014)
 20. Romeo, F., Manevitch, L.I., Bergman, L.A., Vakakis, A.: Transient and chaotic low-energy transfers in a system with bistable nonlinearity. *Chaos* **25**, 053109 (2015)
 21. Romeo, F., Sigalov, G., Bergman, L.A., Vakakis, A.F.: Dynamics of a linear oscillator coupled to a bistable light attachment: numerical study. *J. Comput. Nonlinear Dyn.* **10**(1), 011007 (2015)
 22. Manevitch, L.I., Sigalov, G., Romeo, F., Bergman, L.A., Vakakis, A.: Dynamics of a linear oscillator coupled to a bistable light attachment: analytical study. *J. Appl. Mech.* **81**(4), 041011 (2014)
 23. Manevitch, L.I.: The description of localized normal modes in a chain of nonlinear coupled oscillators using complex variables. *Nonlinear Dyn.* **25**, 95–109 (2001)
 24. Farid, M., Gendelman, O.V.: Tuned pendulum as nonlinear energy sink for broad energy range. *J. Vib. Control* (2015). doi:[10.1177/1077546315578561](https://doi.org/10.1177/1077546315578561)
 25. Cottone, F., Vocca, H., Gammaitoni, L.: Nonlinear energy harvesting. *Phys. Rev. Lett.* **102**, 080601 (2009)
 26. Jia, Y., Seshia, A.A.: Directly and parametrically excited bi-stable vibration energy harvester for broadband operation. *Transducers* (2013). doi:[10.1109/Transducers.2013.6626801](https://doi.org/10.1109/Transducers.2013.6626801)
 27. Harne, R.L., Wang, K.W.: A review of the recent research on vibration energy harvesting via bistable Systems. *Smart Mater. Struct.* **22**, 023001 (2013)
 28. Tang, L.H., Yang, Y.W., Soh, C.K.: Improving functionality of vibration energy harvesters using magnets. *J. Intell. Mater. Syst. Struct.* (2012). doi:[10.1177/1045389X12443016](https://doi.org/10.1177/1045389X12443016)
 29. Gao, Y.J., Leng, Y.G., Fan, S.B., Lai, Z.H.: Studies on vibration response and energy harvesting of elastic-supported bistable piezoelectric cantilever beams. *Acta Phys. Sin.* **63**(9), 090501 (2014)
 30. Vokoun, D., Beleggia, M., Heller, L., Sittner, P.: Magnetostatic interactions and forces between cylindrical permanent magnets. *J. Magn. Magn. Mater.* **321**, 3758–3763 (2009)
 31. Vokoun, D., Beleggia, M., Heller, L.: Magnetic guns with cylindrical permanent magnets. *J. Magn. Magn. Mater.* **324**, 1715–1719 (2012)
 32. Avvari, P.V., Tang, L.H., Yang, Y.W., Soh, C.K.: Enhancement of piezoelectric energy harvesting with multi-stable nonlinear vibrations. *Proc. of SPIE* (2013). doi:[10.1117/12.2009560](https://doi.org/10.1117/12.2009560)
 33. Jones, D.I.G., et al.: *Handbook of Viscoelastic Vibration Damping*. Wiley, Chichester (2001)
 34. Edward, J., Kerwin, M.: Damping of flexural waves by a constrained viscoelastic layer. *J. Acoust. Soc. Am.* **31**(7), 952–962 (1959)
 35. Plunkett, R., Lee, C.T.: Length optimization for constrained viscoelastic layer damping. *J. Acoust. Soc. Am.* **48**, 150–161 (1970)
 36. Hou, S.W., Jiao, Y.H., Wang, X., Chen, Z.B., Fan, Y.B.: Optimization of plate with partial constrained layer damping treatment for vibration and noise reduction. *Appl. Mech. Mater.* **138–139**, 20–26 (2012)
 37. Ling, Z., Ronglu, X., Yi, W., El-Sabbagh, A.: Topology optimization of constrained layer damping on plates using method of moving asymptote (MMA) approach. *Shock Vib.* **18**(1), 221–244 (2011)
 38. Kim, S.Y.: *Topology Design Optimization for Vibration Reduction: Reducible Design Variable Method*. Queen's University, Kingston (2011)
 39. Mead, D.J., Ae, D.C.: The effect of a damping compound on jet-efflux excited vibrations: an article in two parts presenting theory and results of experimental investigation. Part I. The structural damping due to the compound. *Aircr. Eng. Aerosp. Technol.* **32**, 64–72 (1960)
 40. Mead, D.J.: A comparison of some equations for the flexural vibration of damped sandwich beams. *J. Sound Vib.* **83**, 363–377 (1982)
 41. Shi, H.M., Huang, Q.B.: *Vibration Systems: Analyzing, Modeling, Testing, Controlling*. 3rd edn. Huazhong University of science and Technology Press (2014), in Chinese